International Journal of Applied Earth Observation and Geoinformation 128 (2024) 103691

Contents lists available at ScienceDirect

International Journal of Applied Earth Observation and Geoinformation

journal homepage: www.elsevier.com/locate/jag

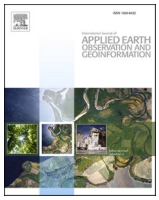

A fast and robust cirrus removal method for Landsat 8/9 images

Tao Jiang [a], Huanfeng Shen [a,b,*], Huifang Li [a,b], Chi Zhang [c,d], Liying Xu [a], Dekun Lin [a]

[a] School of Resource and Environmental Science, Hubei Luojia Laboratory, Wuhan University, Wuhan 430079, China
[b] Collaborative Innovation Center of Geospatial Technology, Wuhan University, Wuhan 430079, China
[c] Guangzhou Urban Planning & Design Survey Research Institute, Guangzhou 510060, China
[d] Guangdong Enterprise Key Laboratory for Urban Sensing, Monitoring and Early Warning, Guangzhou 510060, China

ARTICLE INFO

Keywords:
High-quality cirrus removal
Cirrus parallaxes
Cirrus parallax laws and correction
Automatic sampling
CUDA

ABSTRACT

High-quality cirrus removal plays a crucial role in remote sensing data analysis. Cirrus parallaxes are commonly observed within the vicinity of cirrus clouds in the visible and near-infrared (VNIR) bands of Landsat 8/9 images. Cirrus parallaxes have a nonnegligible effect on cirrus removal, but the existing methods do not account for the correction of parallaxes. Meanwhile, large-scale image processing involves intensive computation that requires extensive computing time. To address the effect of cirrus parallaxes and the low processing efficiency, we propose a fast and robust cirrus removal (FRCR) method. FRCR has achieved the first realization of the statistics law of cirrus parallax between the VNIR and cirrus bands, thus realizing the cirrus parallax correction. In addition, FRCR introduces an automatic sampling method to obtain the regression samples for practicality. Then, a Compute Unified Device Architecture (CUDA) based Newton method with constraints is introduced to parallelize the computation, to improve the computational performance. Experiment results of various scenarios demonstrate that the FRCR method can achieve high-quality cirrus removal by eliminating cirrus parallaxes, and significantly improving computational performance.

1. Introduction

Cirrus clouds, as a typical type of optically thin cloud(Meyer et al., 2004; McHardy et al., 2022), are composed of ice crystal particles and a small number of gas molecules (Dowling and Radke, 1990). Cirrus cloud is partly transparent and difficult to detect with common broadband multispectral sensors (Richter et al., 2011). Various radar-based detection methods (Sassen and Cho, 1992; Winker et al., 2007; Young et al., 2018; McHardy et al., 2022) have been proposed to detect cirrus clouds, providing a reliable database for meteorological studies worldwide. Additionally, some multispectral remote sensing satellite sensors are equipped with the cirrus band (Dessler and Yang, 2003; Drusch et al., 2011; Zanter, 2016; Masek et al., 2020). Since the absorption and scattering of ice crystals by cirrus cloud modulates the transportation of radiation through the Earth's atmosphere, the atmospheric effect can cause inaccurate or deceptive analysis of land surface and environmental observations(Xu et al., 2014). Therefore, cirrus removal is essential for enhancing the quality of satellite images.

There have been many methods developed for removing thin clouds, including the subtraction methods of dark objects (Chavez, 1988; Makarau et al., 2014), the methods based on image transformation (Chen et al., 2015; He et al., 2010; Zhang et al., 2002), and frequency domain filtering methods (Du et al., 2002; Mitchell et al., 1977; Shen et al., 2014). In the field of dark target methods, Chavez (1988) counted the lowest reflectance value in the whole image band by band and subtracted it from the corresponding band, treating it as the thin cloud interference, so that the radiance bias caused by the cloud could be eliminated and the actual surface reflectance could be obtained. The most well-known image transformation-based method is haze-optimized transformation (HOT) (Zhang et al., 2002). HOT found that the red and blue bands of the images have a strong linear correlation when the sky is clear, and that this relationship breaks down when clouds are present. Therefore, it is possible to achieve thin cloud removal by adjusting the cloud pixels to a clear skyline. As for the frequency domain filtering methods, they treat clouds as low-frequency noise. For example, Shen et al. (2014) used homomorphic filtering to suppress the low-frequency features that reflect the cloud component while enhancing the high-frequency features that reflect the surface information. However, accurately estimating the reflectance of thin clouds in the visible and near-infrared (VNIR) spectral bands remains a significant challenge in remote sensing. This is primarily due to the complex and diverse nature of thin cloud composition. Thin clouds are often a complex

* Corresponding author.
E-mail address: shenhf@whu.edu.cn (H. Shen).

https://doi.org/10.1016/j.jag.2024.103691
Received 15 November 2023; Received in revised form 19 January 2024; Accepted 26 January 2024
Available online 28 February 2024

Table 1
Landsat 8/9 OLI experimental data.

Scene	Path/row	Image type	Acquisition date	Country
1	89/83	Cloudy image	2013–10-04	Australia
		Reference image	2013–09-18	
2	119/38	Cloudy image	2021–01-14	China
		Reference image	2021–01-30	
3	123/39	Cloudy image	2021–11-26	China
		Reference image	2021–11-10	
4	129/43	Cloudy image	2020–01-02	China
		Reference image	2020–01-18	

amalgamation of different cloud types, characterized by multifaceted and complicated attributes.

Recently, some methods for removing cirrus clouds have been developed by utilizing the cirrus band, which is the band carried by optical satellites for detecting cirrus clouds, with a central wavelength of 1.38 μm and strong water vapor absorption properties(Gao et al., 1993). In general, estimating cirrus reflectance in each band by assuming a linear relationship among bands is common in traditional cirrus removal methods (Gao et al., 1998; Gao et al., 2002; Xu et al., 2014; Lv et al., 2016). However, these methods are limited by homogeneous scenarios and linear fitting sample selection. There are also methods for image transformation, mainly integrating VNIR bands with the cirrus band, and using component analysis techniques to separate the cloud component components to be used for cirrus removal (Shen et al., 2015; Xu et al., 2019), such as Shen et al. (2015) proposed an independent component analysis (ICA) based method to correct for thin clouds. Xu et al. (2019) proposed a thin cloud removal method based on a noise-adjusted principal components transform (CR-NAPCT) model. However, the methods lack an explicit physical property, and the performance is not satisfactory in some complex scenarios, sometimes the post-process may be required to obtain satisfactory results in cirrus removal. For the consideration of scattering law and applicability of cirrus removal methods, Zhang et al. (2021) proposed a scattering law-based cirrus correction (SLCC) method, which couples band correlation with a scattering model to achieve high-fidelity removal of thin cirrus cloud. The SLCC method is suitable for almost all thin cirrus removal scenarios and has a high degree of universality. The SLCC method is suitable for almost all thin cirrus removal scenarios and has a high degree of universality. However, this method does not take into account the impact of cirrus parallax. It uses a pixel-by-pixel solution to the parameters but does not consider an effective means of optimization, resulting in low efficiency when processing the whole image.

Various methods have been developed to remove cirrus clouds, but their efficiency and parallax correction still need to be investigated. Aiming at low-efficiency issues, Graphics processing units (GPUs) are designed for image processing and have a large number of parallel processing units (typically hundreds to thousands), which provide excellent performance when processing large amounts of data (Lindholm et al., 2008; Nickolls and Dally, 2010; Owens et al., 2008). GPU-based parallel computing has recently been used to improve the computational efficiency for remote sensing data, such as synthetic aperture radar (SAR) simulation (Balz and Stilla, 2009), image classification (Wu et al., 2015; Wu et al., 2017), hyperspectral unmixing (Plaza et al., 2011; Jaramago et al., 2019), and spatio-temporal data fusion (Gao et al., 2022; Yang et al., 2022). These are all large and intensive computing tasks that are suitable for parallel processing. For example, Plaza et al. (2011) developed a high-performance hyperspectral unmixing technique based on a GPU platform. GPU-based parallelism has since become indispensable in improving the computational efficiency in remote sensing.

Besides the low efficiency, another issue is the absence of correction for cirrus parallaxes. Cirrus parallaxes have a significant effect on thin cirrus removal methods (Richter et al., 2011; Gao and Li, 2017; Zhang et al., 2023). It has been found even the presence of 1 pixel of cirrus parallax can degrade the cloud removal quality. (Richter et al., 2011). Therefore, correcting for cirrus parallax is essential to achieve a high-quality thin cirrus removal.

In this study, to address the above issues of cirrus parallax, method inefficiency, and practicality, we proposed a fast and robust cirrus removal (FRCR) method that considers not only the parallaxes but also the computational performance. Firstly, we further developed the physical scattering model and utilized statistical methods to count the cirrus parallax laws of Landsat 8 Operational Land Imager (OLI) (Zanter, 2016) and Landsat 9 Operational Land Imager-2 (OLI-2) (Masek et al., 2020) data, thus completing the correction of cirrus parallaxes. Secondly, we introduced an automatic sampling method based on a box plot to enhance the usability of the cirrus removal method. Then, we proposed a Compute Unified Device Architecture (CUDA) based Newton method with constraints to solve parameters for parallelizing intensive computation to enhance computational efficiency. Finally, a fast, robust, and high-quality cirrus removal method for remote sensing images was achieved.

2. Data

The study used Landsat 8 OLI data and Landsat 9 OLI-2 data. For simplicity, Landsat 8/9 OLI will be used throughout the paper. Landsat 8/9 OLI data can be obtained from the U.S. Geological Survey (USGS; https://earthexplorer.usgs.gov), which consists of nine spectral bands, including a pan band. In this study, the VNIR and cirrus bands were mainly used, including coastal aerosol band (0.435–0.451 μm), blue band (0.452–0.512 μm), green band (0.533–0.590 μm), red band (0.636–0.673 μm), near-infrared band (0.851–0.879 μm), and cirrus band (1.363–1.384 μm). The top-of-atmosphere (TOA) reflectance is effective in minimizing the disparities between scenes and adjusting for the shape of the solar spectrum to amplify the spectral contrasts between cloud spectra and other end elements (Chander et al., 2009). TOA reflectance can be calculated using the equation provided in the official User's Handbook (Zanter, 2016). The satellite view azimuth angle data is also used which could be obtained from the Landsat 8/9 Collection 2 Level-1(C2 L1) products, e.g., LC08_L1TP_089083_20131004_20200912_02_T1_ANG.txt. This file contains per-pixel solar and sensor azimuth and zenith values of each spectral band.

Quantitatively evaluating cloud removal methods is challenging due to the difficulty of obtaining both cloudy and cloud-free images of the same scene simultaneously (Xu et al., 2015). Therefore, we assumed that there was little feature variation between adjacent time phases of cloud-free and cloudy images, with only the atmospheric conditions differing. Four different scenes, consisting of both cloudy and cloud-free images acquired during adjacent time phases, were selected as the experimental data, as shown in Table 1, where cloud-free images are reference images.

3. Methods

3.1. Scattering law-based cirrus removal

The cloudy image model can be expressed simply as follows (Chavez, 1988; Xia et al., 2018; Zhang et al., 2021):

$$\rho^*(\lambda) = \rho_c(\lambda) + \rho(\lambda)\cdot T_c(\lambda) \tag{1}$$

where ρ^* is the cloudy image TOA reflectance, λ is the band central wavelength, $\rho_c(\lambda)$ is the cirrus reflectance, $\rho(\lambda)$is the reflectance of the ground under the cirrus cloud, and $T_c(\lambda)$ is the two-way transmittance through the cirrus cloud. To obtain a clean image, it is necessary to calculate $\rho_c(\lambda)$ and $T_c(\lambda)$. T_c is typically greater than 0.9, which can be approximated as 1(Gao et al., 1998; Richter et al., 2011). Therefore, it is only necessary to compute $\rho_c(\lambda)$ to obtain the cloud-free image $\rho(\lambda)$.

To solve $\rho_c(\lambda)$, we introduce the Angstrom exponent (Gordon and Wang, 1994; Mao et al., 2013) to express the relationship between the

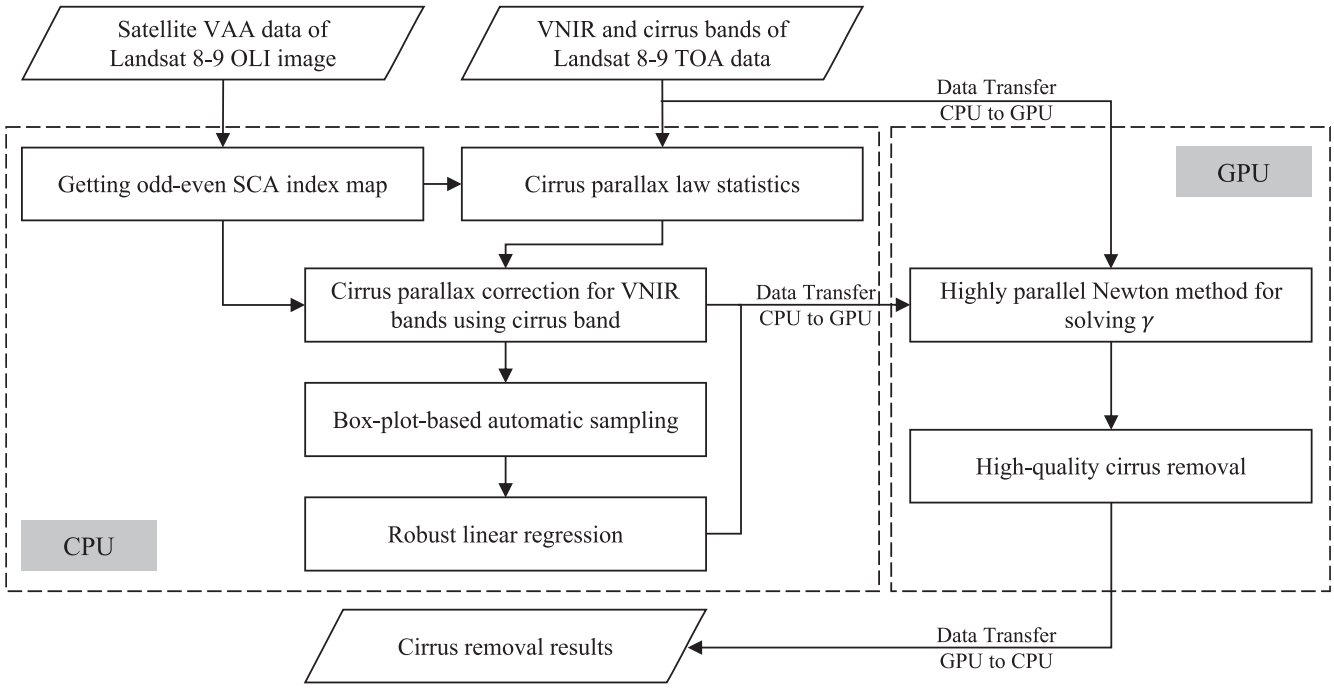

Fig. 1. The flowchart of the FRCR method.

Table 2
Device and Software Information.

	Specification	Details
CPU	Processor number	Intel Core i7-9700 K
	Processor base frequency	3.60 GHz
	Cores	8
	Memory	64 GB
GPU	Graphics card	NVIDIA GeForce RTX 2070
	GPU architecture	Turing
	Compute capability	7.5
	Maximum threads per block	1024
	Maximum number of threads per SM	1024
	Memory bus width	256-bit
	Clock rate	1.65 GHz
	Memory clock rate	7001 MHz
	CUDA version	11.6
	CUDNN version	8.8.0

cirrus reflectance and wavelength in each band, as shown in Eq. (2):

$$\rho_c(\lambda_i) = \left(\frac{\lambda_j}{\lambda_i}\right)^{\gamma} \cdot \rho_c(\lambda_j) \tag{2}$$

where i or j is the band number, belonging to 1, 2, 3, 4, 5, or 9, γ represents the Angstrom exponent related to the atmospheric state, belonging to [0, 4] (Chavez, 1988), where 0 is very cloudy and 4 is very clean.

The atmospheric state is spatially the same for a pixel, so γ can be considered a constant for the Landsat 8/9 VNIR and cirrus bands. Hence, given the knowledge of the cirrus reflectance in band i, it is possible to determine the cirrus reflectance in band j. In general, when cirrus clouds are present, the ground reflectance in the cirrus band is almost zero (Gao et al., 1993; Zhang et al., 2021), so $\rho^*(\lambda_9)$ is equal to $\rho_c(\lambda_9)$. Therefore, the cirrus reflectance for each band i can be calculated according to Eq. (3).

$$\rho_c(\lambda_i) = \left(\frac{\lambda_9}{\lambda_i}\right)^{\gamma} \cdot \rho_c(\lambda_9) \tag{3}$$

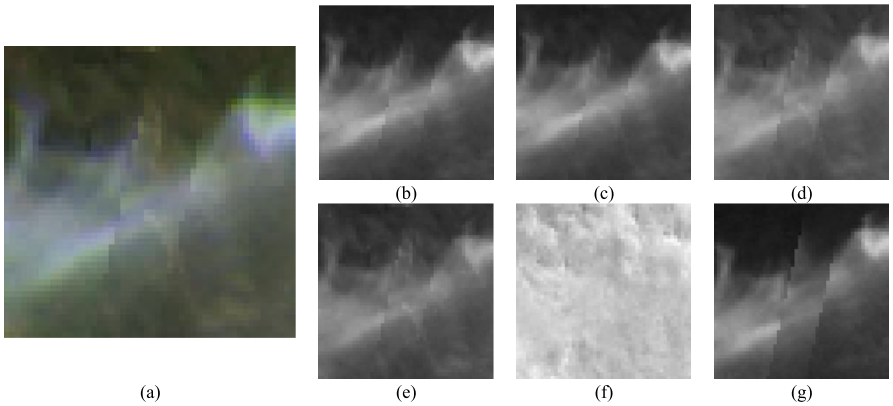

Fig. 2. (a)The OLI sub-image shown in RGB (path = 89, row = 83, acquisition date = 20131004, R = Band 4, G = Band 3, B = Band 2). (b)Coastal aerosol band, (c) Blue band, (d)Green band, (e)The Red Band, (f)Near-Infrared band, (g)Cirrus band. (For interpretation of the references to color in this figure legend, the reader is referred to the web version of this article.)

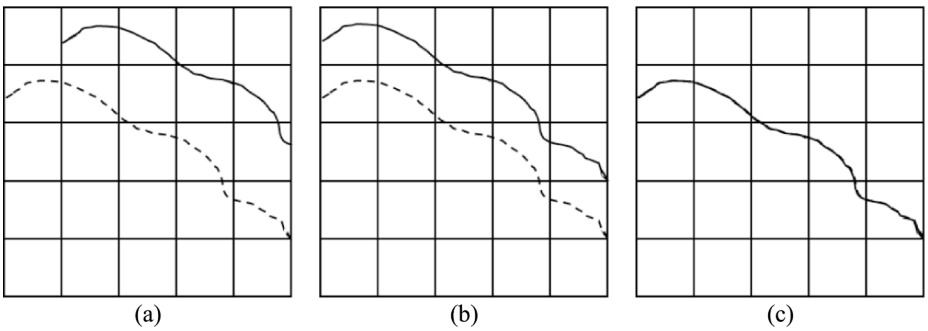

Fig. 3. (a)Cirrus position in a VNIR band (dashed line) and cirrus band (solid line), respectively, (b)Position of the cirrus after correction to the left, (c)The position of cirrus in the corrected VNIR band and cirrus band.

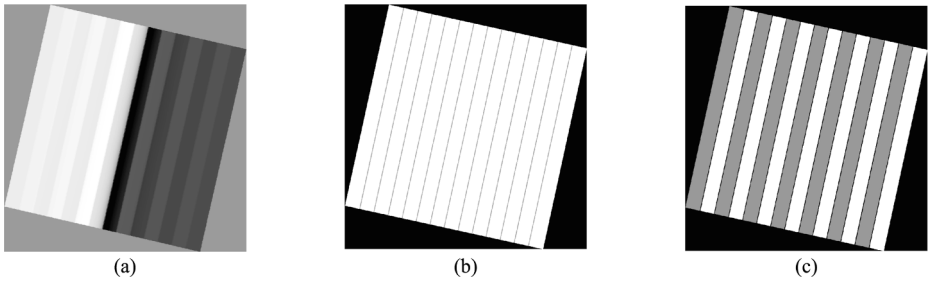

Fig. 4. (a)Landsat 8/9 OLI original satellite view azimuth angle data, (b)Results of l8_angles processing(c)Index map of odd–even SCAs.

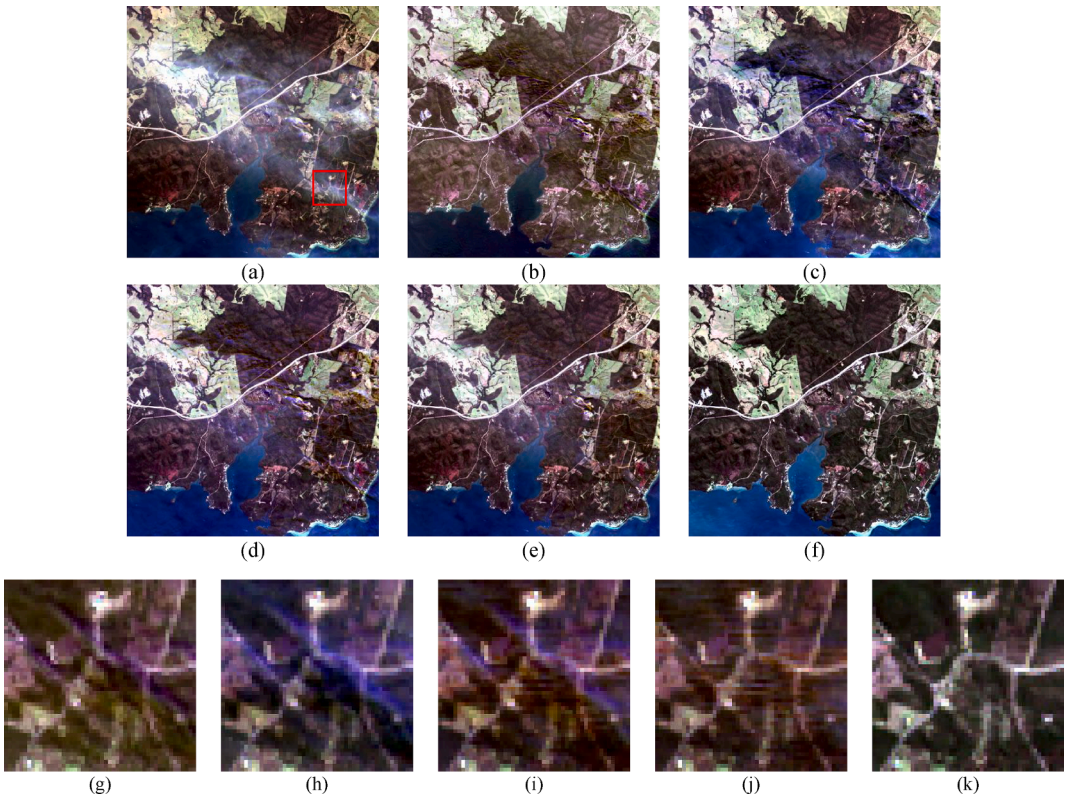

Fig. 5. The cloudy image, cirrus removal results for each method and cloud-free image of adjacent time phase in Scene 1 sub-image shown in RGB, (a)Cloudy image, (b)ICA. (c) CR-NAPCT, (d)SLCC, (e)FRCR, (f)Cloud-free reference image, (g)–(k)denote the zoomed red region of Fig. 5, (b)–(f). (For interpretation of the references to color in this figure legend, the reader is referred to the web version of this article.)

Therefore, it is crucial to find out how to solve for γ. A coupled band relationship and scattering model (Zhang et al., 2021) was proposed for solving γ. This is because the Landsat 8/9 OLI coastal aerosol band is similar in wavelength to the blue band, and there is a sharp linear correlation in the cloud-free land surface region (Lv et al., 2016; Zhang et al., 2021), as follows,

Table 3
Quantitative evaluation of cirrus removal results for each sub-scene data.

Scene	Method	SAM					SSIM				
		Band 1	Band 2	Band 3	Band 4	Band 5	Band 1	Band 2	Band 3	Band 4	Band 5
1	Cloudy	0.0886	0.1076	0.1273	0.1575	0.0787	0.9901	0.9858	0.9794	0.9690	0.9693
	ICA	0.1182	0.4039	1.8341	2.1510	0.2939	0.6480	0.3585	−0.1593	−0.5322	0.6776
	CR-NAPCT	0.0484	0.0650	0.0967	0.1728	0.1737	0.9950	0.9925	0.9796	0.9341	0.7769
	SLCC	0.0414	0.0566	0.0723	0.1036	**0.0719**	0.9972	0.9963	0.9957	**0.9921**	**0.9745**
	FRCR	**0.0365**	**0.0494**	**0.0718**	**0.1025**	0.0721	**0.9985**	**0.9978**	**0.9959**	0.9920	0.9744
2	Cloudy	0.1414	0.1591	0.1768	0.1935	0.1780	0.9756	0.9697	0.9629	0.9463	0.9234
	ICA	0.0584	0.0725	0.0935	0.1183	0.1575	0.8810	0.8560	0.8226	0.7887	0.8006
	CR-NAPCT	**0.0514**	0.0707	0.0918	0.1258	0.1583	0.9797	0.9739	0.9707	0.9652	0.9440
	SLCC	0.0583	0.0734	0.0888	0.1180	0.1417	0.9884	0.9850	0.9841	0.9744	0.9461
	FRCR	0.0570	**0.0701**	**0.0888**	**0.1176**	**0.1412**	**0.9910**	**0.9884**	**0.9850**	**0.9751**	**0.9466**
3	Cloudy	0.1132	0.1388	0.1718	0.2305	0.1350	0.9801	0.9731	0.9672	0.9396	0.9434
	ICA	0.0492	0.0742	0.1307	0.2461	0.1509	0.8554	0.8088	0.7614	0.6544	0.8986
	CR-NAPCT	0.0556	0.0741	0.1003	0.1547	0.1233	0.9913	0.9885	0.9876	0.9733	0.9469
	SLCC	0.0411	0.0572	0.0752	0.1251	0.1187	0.9948	0.9934	0.9935	**0.9831**	0.9490
	FRCR	**0.0358**	**0.0497**	**0.0740**	**0.1233**	**0.1185**	**0.9958**	**0.9946**	**0.9935**	0.9828	**0.9493**
4	Cloudy	0.1555	0.1848	0.2040	0.2645	0.2775	0.8980	0.8784	0.8766	0.8462	0.7079
	ICA	0.1013	0.1233	0.1395	0.2386	0.4249	0.9631	0.9546	0.9544	0.8745	0.5992
	CR-NAPCT	0.0922	0.1104	0.1233	0.1554	0.2179	0.9747	0.9632	0.9454	0.9531	0.7687
	SLCC	0.0951	0.1152	0.1245	0.1594	0.1984	0.9809	0.9761	0.9730	0.9549	0.7912
	FRCR	**0.0872**	**0.1088**	**0.1230**	**0.1408**	**0.1959**	**0.9843**	**0.9805**	**0.9738**	**0.9579**	**0.7954**

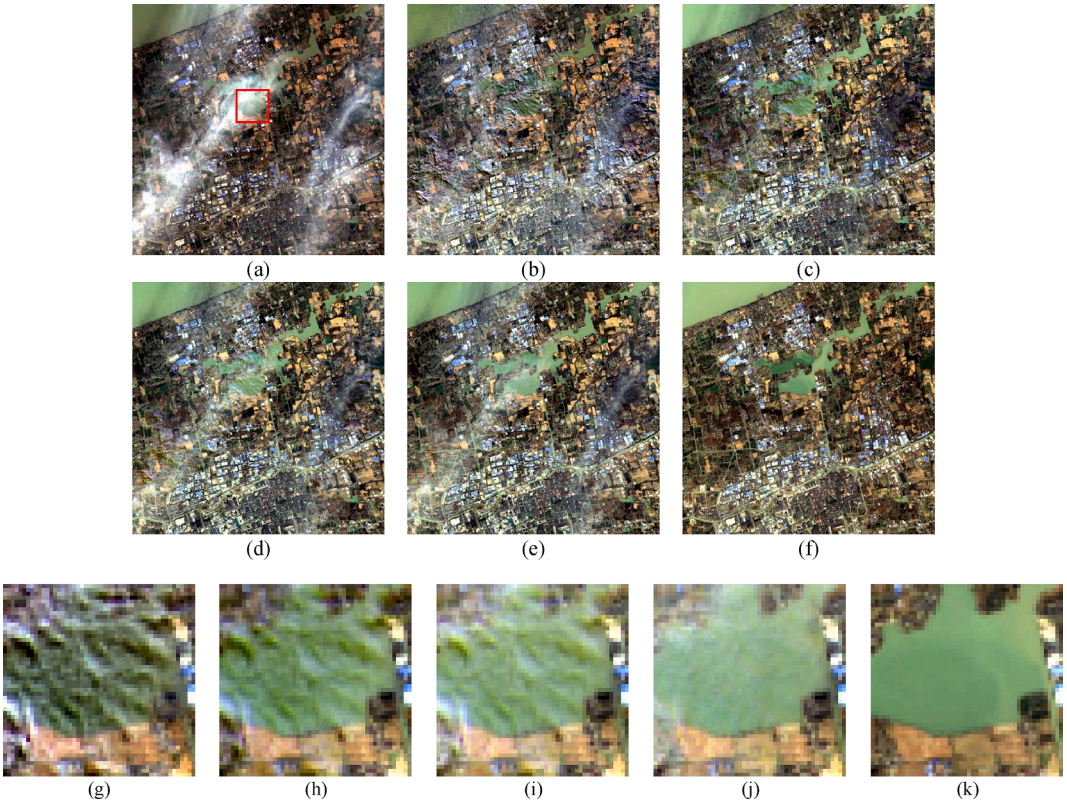

Fig. 6. The cloudy image, cirrus removal results for each method and cloud-free image of adjacent time phase in Scene 2 sub-image, (a)Cloudy image, (b)ICA, (c)CR-NAPCT, (d)SLCC, (e)FRCR, (f)Cloud-free reference image, (g)–(k)denote the zoomed red region of Fig. 6. (b)–(f). (For interpretation of the references to color in this figure legend, the reader is referred to the web version of this article.)

$$\rho(\lambda_1) = a \cdot \rho(\lambda_2) + b \tag{4}$$

where λ_1 represents the coastal aerosol band, λ_2 represents the blue band, a and b represent the coefficients of the linear regression. Then, the following equations can be obtained.

$$\rho^*(\lambda_1) = \rho_c(\lambda_1) + \rho(\lambda_1)$$

$$\rho^*(\lambda_2) = \rho_c(\lambda_2) + \rho(\lambda_2)$$

$$\rho_c(\lambda_1) = \left(\frac{\lambda_9}{\lambda_1}\right)^{\gamma} \cdot \rho_c(\lambda_9)$$

$$\rho_c(\lambda_2) = \left(\frac{\lambda_9}{\lambda_2}\right)^{\gamma} \cdot \rho_c(\lambda_9) \tag{5}$$

Combining Eqs. (4) and (5), γ can be solved by a two-sided approximation method with a step size of 0.01 (Zhang et al., 2021), but it is time-consuming to solve for all the image pixels.

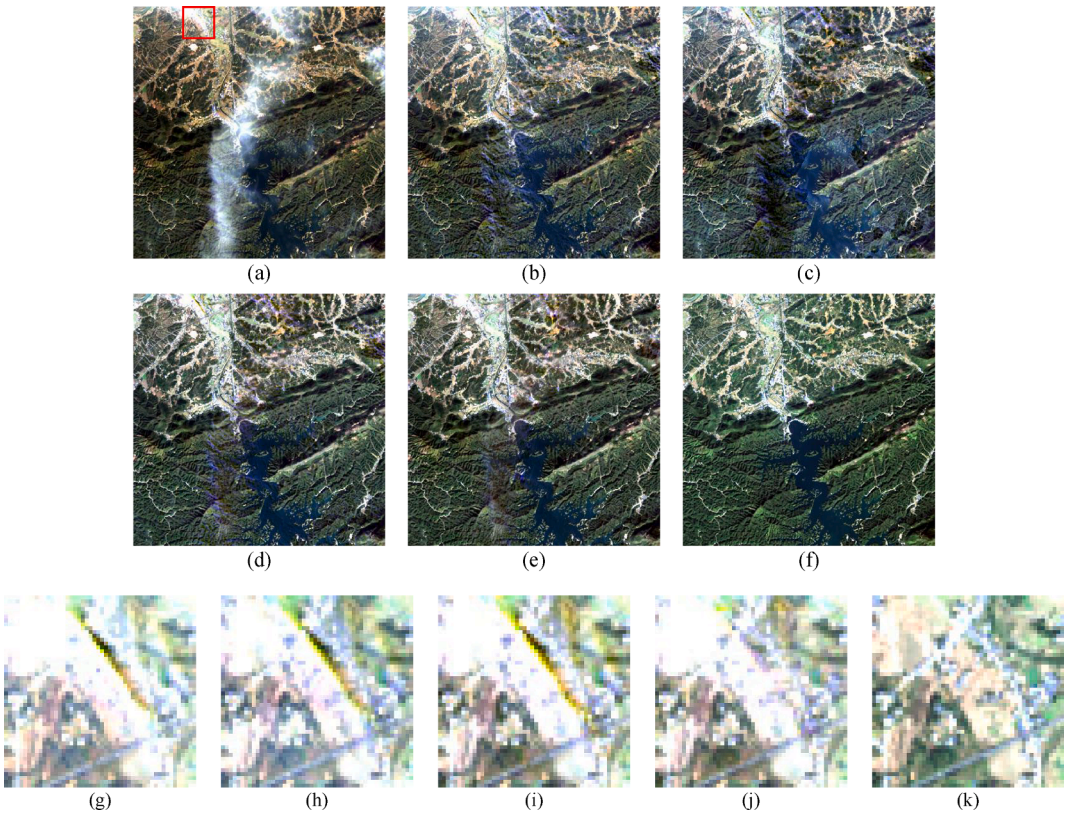

Fig. 7. The cloudy image, cirrus removal results for each method and cloud-free image of adjacent time phase in Scene 3 sub-image, (a)Cloudy image, (b)ICA, (c)CR-NAPCT, (d)SLCC, (e)FRCR, (f)Cloud-free reference image, (g)–(k)denote the zoomed red region of Fig. 7. (b)–(f). (For interpretation of the references to color in this figure legend, the reader is referred to the web version of this article.)

3.2. Proposed fast and robust cirrus removal (FRCR) method

The implementation of the FRCR method is described in this section. There are three main steps in the FRCR method, as shown in Fig. 1, which are: 1) an automatic sampling method based on box plots has been introduced as a replacement for manual sampling in regression analysis; 2) the solution for γ is reconstructed using the Newton method based on the CUDA, which is an NVIDIA-developed parallel computing model (https://developer.nvidia.com/cuda-toolkit) for general GPU computation and parallelization; and 3) the proposed method takes into account the cirrus parallaxes and uses a statistical method to count the cirrus parallax law, and then the law is employed to correct the cirrus parallax for VNIR bands based on the cirrus band.

3.2.1. Box-plot-based automatic sampling

It is recognized that the coastal aerosol bands of OLI data have similar wavelengths to the blue band, and they show a strong linear relationship at the cloud-free land surface regions. Nonetheless, the correlation between the two bands varies considerably among images. Cloud-free pixels should be selected as samples for all Landsat 8/9 image processing. In general, the regression samples are usually selected manually to ensure diversity and homogeneity of pixels. However, we propose an empirical threshold filtering method based on box plots to obtain accurate samples automatically. The method initially sets an empirical threshold (τ) for the TOA reflectance value for the cirrus band, where pixels larger than τ are considered cloudy; otherwise, they are considered cloud-free. It was determined from comprehensive statistical analysis in this study that by setting τ equal to 0.0012, more accurate and cleaner pixels can be acquired. Then, according to the threshold, we segment the cirrus band into cloudy and cloud-free areas, where the cloudy area is recorded as logical value 1, and the cloud-free area is recorded as 0. Consequently, the cloudy and cloud-free index map consists of logical values 0 and 1. Initial sample data $S^{'}$ can be derived from this map. Furthermore, we utilize the box plot method to clean $S^{'}$. The upper and lower whiskers of the box plot are recognized as the limits of the data distribution. The data over the upper or lower whiskers are outliers and need to be eliminated. Therefore, the final sample S is obtained. Finally, we introduce robust linear regression (Holland and Welsch, 1977) to fit S to obtain a and b.

3.2.2. Cuda-based parallel Newton method for solving γ

In contrast to the fixed-step iterative solution, we further derive Eq. (5) as Eq. (6) and introduce the Newton method to solve γ as follows:

$$a\cdot\left(\frac{\lambda_9}{\lambda_2}\right)^{\gamma}-\left(\frac{\lambda_9}{\lambda_1}\right)^{\gamma}=\frac{a\cdot\rho^{*}(\lambda_2)+b-\rho^{*}(\lambda_1)}{\rho_c(\lambda_9)} \tag{6}$$

where a and b can be obtained in Eq. (4), and then it is only necessary to solve for γ.

Based on Eq. (6), the function $F(\gamma)$ can be constructed in terms of γ, where γ belongs to [0,4]. It can be seen from Eq. (7) that $F(\gamma)$ contains two exponential functions and a constant. The Newton method is used to solve for the optimal γ value, which is an iterative optimization algorithm for solving nonlinear equations or optimization problems with fast convergence and global search capability.

$$F(\gamma)=a\cdot\left(\frac{\lambda_9}{\lambda_2}\right)^{\gamma}-\left(\frac{\lambda_9}{\lambda_1}\right)^{\gamma}-\frac{a\cdot\rho^{*}(\lambda_2)+b-\rho^{*}(\lambda_1)}{\rho_c(\lambda_9)} \tag{7}$$

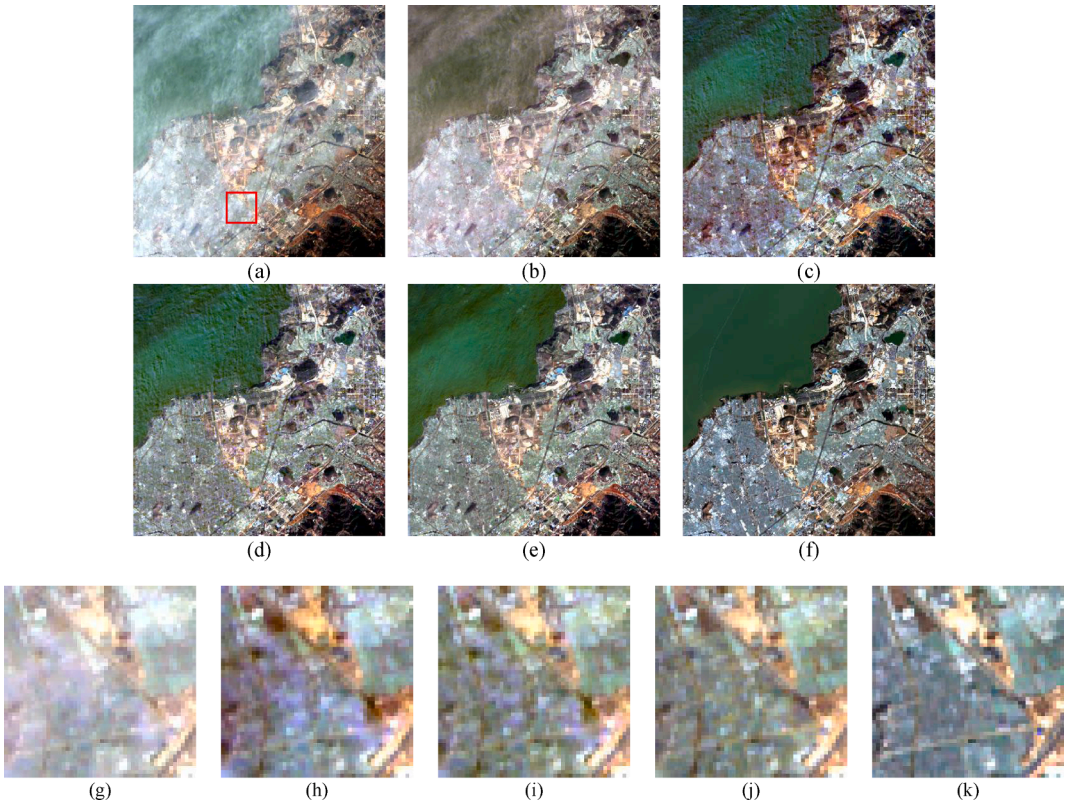

Fig. 8. The cloudy image, cirrus removal results for each method and cloud-free image of adjacent time phase in Scene 4 sub-image, (a)Cloudy image, (b)ICA, (c)CR-NAPCT, (d)SLCC, (e)FRCR, (f)Cloud-free reference image, (g)–(k)denote the zoomed red region of Fig. 8. (b)–(f). (For interpretation of the references to color in this figure legend, the reader is referred to the web version of this article.)

When $F(\gamma) = 0$, it is possible to obtain the first-order derivative Taylor expansion of $F(\gamma)$.

$$F(\gamma) = F(\gamma_0) + F^{'}(\gamma_0)(\gamma - \gamma_0) \tag{8}$$

It is usually assumed that γ_1 is closer to the solution $F(\gamma) = 0$ than γ_0, and the next iteration is started with γ_1. The iteration formula can be simplified as follows:

$$\gamma_{n+1} = \gamma_n - \frac{F(\gamma_n)}{F^{'}(\gamma_n)} \tag{9}$$

$$s.t.\ \gamma_{n+1} = \max(0, \min(4, \gamma_{n+1})) \text{ and } 0 \le \gamma_{n+1} \le 4 \tag{10}$$

The primary objective of parallel implementation is to transfer the time-intensive components to the GPU execution. In addition, it is necessary to pay attention to the optimization and allocation of memory, reducing the input and output (I/O) transfer frequency between the central processing units (CPUs) and the GPUs (Wu et al., 2017). As the atmospheric state constant γ varies for each pixel, it is essential to solve for γ pixel by pixel, and the solutions corresponding to each pixel are independent. However, this is time-consuming for the whole Landsat 8/9 image processing in CPUs. In this study, we found that the best approach was to assign the computation of each pixel to a separate thread to achieve a parallel solution for each image pixel and improve the efficiency of the method. Thus, we designed a GPU-based parallel Newton method for solving γ. The method pseudocode is shown in Algorithm 1.

Algorithm 1. CUDA-based parallel Newton method for solving γ

Input: TOA of Coastal band $\rho^*(\lambda_1)$, TOA of Blue band $\rho^*(\lambda_2)$, TOA of Cirrus band $\rho^*(\lambda_9)$, center wavelength of Coastal band λ_1, Blue band λ_2 and Cirrus band λ_9, Linear fitting parameters a, b
Output: Atmospheric state constant γ

(*continued on next column*)

(*continued*)

Algorithm 1. CUDA-based parallel Newton method for solving γ

Initialisation: *maxIterations*←100, γ_0←2.0, ϵ←$1e-6$
For each pixel **do**
col←threadIdx.x + blockIdx.x × blockDim.x;
row←threadIdx.y + blockIdx.y × blockDim.y;
If (col < width) and (row < height) **then**
tid←*col* + *row* × *width*;
//Allocation of shared memory based on wrap
$\rho^*_{shared}(\lambda_1)[32][32]$; $\rho^*_{shared}(\lambda_2)[32][32]$; $\rho^*_{shared}(\lambda_9)[32][32]$;
//Load frequently used arrays into shared memory to minimise global memory accesses
$\rho^*_{shared}(\lambda_1)$[threadIdx.y][threadIdx.x]←$\rho^*(\lambda_1)[tid]$;
$\rho^*_{shared}(\lambda_2)$[threadIdx.y][threadIdx.x]←$\rho^*(\lambda_2)[tid]$;
$\rho^*_{shared}(\lambda_9)$[threadIdx.y][threadIdx.x]←$\rho_c(\lambda_9)[tid]$;
synchronize threads within the block
For*i*←0*tomaxIterations***do**

$$f \leftarrow F\begin{pmatrix} \gamma_0, a, b, \lambda_1, \lambda_2, \lambda_9, \\ \rho^*_{shared}(\lambda_1)[\text{threadIdx.y}][\text{threadIdx.x}], \\ \rho^*_{shared}(\lambda_2)[\text{threadIdx.y}][\text{threadIdx.x}], \\ \rho^*_{shared}(\lambda_9)[\text{threadIdx.y}][\text{threadIdx.x}] \end{pmatrix};$$

$f^{'} \leftarrow F^{'}(\gamma_0, a, \lambda_1, \lambda_2, \lambda_9)$;
$\Delta\gamma_0 \leftarrow f/f^{'}$;
$\gamma_0 \leftarrow \gamma_0 - \Delta\gamma_0$;
$\gamma_0 \leftarrow \max(0, \min(4, \gamma_0))$;
If $\Delta\gamma_0 < \epsilon$ **then**
break;
$\gamma[threadId] \leftarrow \gamma_0$;

The main parts of Algorithm 1 are as follows

1) Optimization of the memory I/O transfers: In this study, we focused on optimizing the data communication between the CPU and GPU to minimize the data transfer overhead. Once the data were in the GPU,

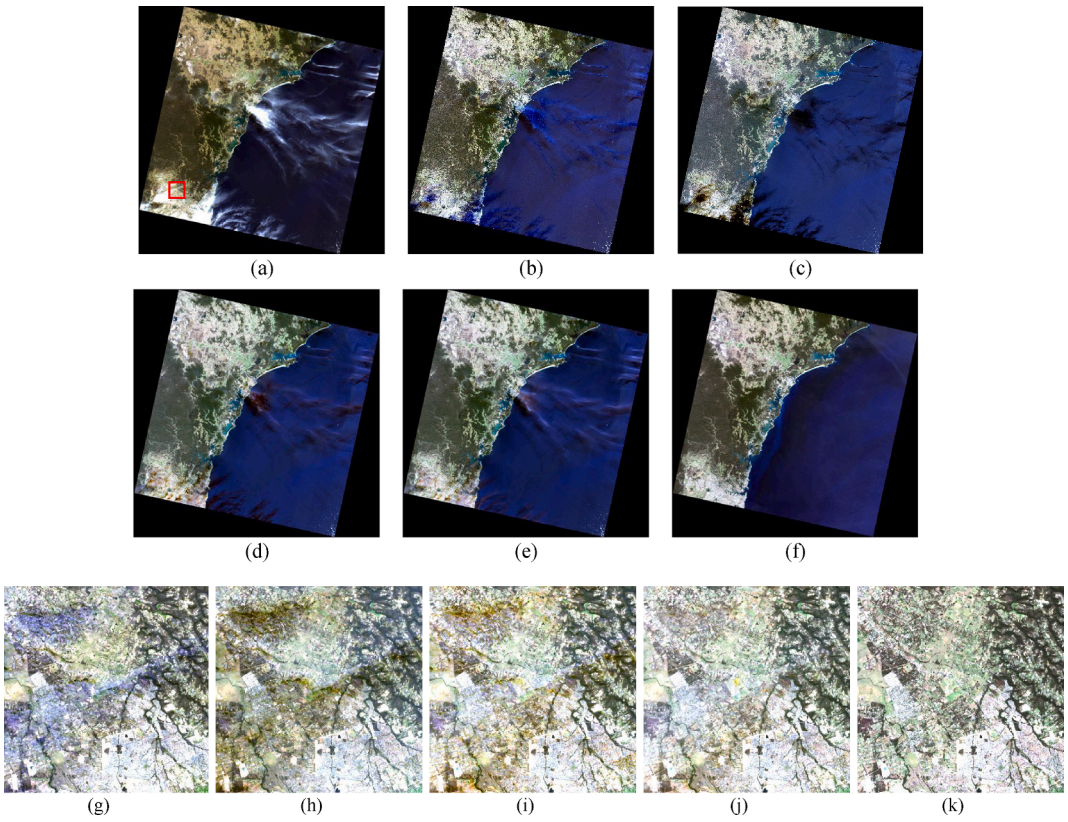

Fig. 9. The cloudy image, cirrus removal results for each method and cloud-free image of adjacent time phase in the whole Scene 4 image, (a)Cloudy image, (b)ICA, (c)CR-NAPCT, (d)SLCC, (e)FRCR, (f)Cloud-free reference image, (g)–(k)denote the zoomed red region of. (For interpretation of the references to color in this figure legend, the reader is referred to the web version of this article.)

Table 4
Quantitative evaluation of cirrus removal results for the whole scene 1 image.

Scene	Method	SAM					SSIM				
		Band 1	Band 2	Band 3	Band 4	Band 5	Band 1	Band 2	Band 3	Band 4	Band 5
1	Cloudy	0.1627	0.2125	0.3133	0.4301	0.2941	0.9842	0.9779	0.9622	0.9378	0.8485
	ICA	0.0943	0.1376	0.2538	0.3917	0.3008	0.9870	0.9816	0.9666	0.9383	0.8191
	CR-NAPCT	0.1261	0.1757	0.2857	0.4208	0.2969	0.9859	0.9803	0.9677	0.9469	0.8613
	SLCC	0.0995	0.1443	0.2523	0.3788	0.2835	0.9889	0.9847	0.9744	0.9572	0.8704
	FRCR	**0.0934**	**0.1382**	**0.2482**	**0.3762**	**0.2834**	**0.9893**	**0.9851**	**0.9745**	**0.9583**	**0.8722**

Table 5
Time to solve γ for data of different sizes (unit: seconds).

Methods	400 × 400	800 × 800	1600 × 1600	3200 × 3200	Raw Size
SLCC	2.553	8.634	39.517	163.273	816.629
FRCR	0.621	2.411	9.777	39.155	152.185
FRCR (with OpenMP)	0.208	0.588	1.654	6.599	23.072
FRCR (with GPU)	**3.74E-04**	**1.62E-03**	**5.42E-03**	**1.67E-02**	**0.111**

Table 6
Total runtime of the program for data of different sizes (unit: seconds).

Methods	400 × 400	800 × 800	1600 × 1600	3200 × 3200	Raw size
ICA	0.919	28.557	50.863	115.049	2516.491
CR-NAPCT	**0.131**	0.478	1.832	7.932	51.750
SLCC	2.696	9.696	40.807	167.312	832.766
FRCR	0.285	**0.416**	**0.918**	**2.824**	**18.255**

we used the shared memory mechanism to cache frequently accessed arrays, thereby reducing the frequency of the global memory accesses. This optimization strategy improves the execution efficiency of GPU kernels.

2) Dynamic allocation of kernel function threads: From a hardware perspective, the streaming processor (SP), which is also called the CUDA core, is the fundamental processing unit of a GPU. The streaming multiprocessor (SM) is assembled utilizing several CUDA cores, where CUDA cores in each SM are related to the GPU architecture, with a count of 1024 CUDA cores per SM for the Turing architecture examined in this study, as shown in Table 2. A single-instruction multiple-thread (SIMT) architecture is utilized by the SM, with a warp (a bundle of threads) serving as the fundamental execution unit. Each warp carries out identical instructions with varying data resources across 32 parallel threads. Considering that the standard size of a warp is 32, blocks typically consist of a multiple of 32 threads. The maximum thread number per block is 1024, if block.x of a block is 1024, then block.y must be 1, and vice versa. In other cases, ensuring that a multiple of 32 is advisable. To execute a

kernel function on the GPU, only one grid can be used, where thread block numbers called in this grid are correlated with the input data, and calculated as grid.x $=(\text{width}+\text{block.x}-1)//\text{block.x}$, and grid.y $=(\text{height}+\text{block.y}-1)//\text{block.y}$, where the width and height are the columns and rows of the input data, respectively.

3) Parallel implementation for solving γ: The method unrolls the pixel loop, allocating each pixel to a thread in the thread blocks within the employed GPU grid. Since the input data size determines the threads initialized by the kernel, it is ensured that each element of the image is assigned to a thread, resulting in parallelization.

3.2.3. Statistics laws and correction of cirrus parallaxes

The parallax problem is usually because different spectral bands are set up within the focal plane module, and each spectral band is viewed at a different angle, causing them to be biased when recording the same ground feature (Richter et al., 2011; Gao and Li, 2017). A cirrus parallax image is unfolded band by band, and then the shape and position of the cirrus clouds on each band are observed and analyzed, as shown in Fig. 2. It can be found that the cirrus parallax is especially obvious in the presence of sharp cloud edges, and the cirrus parallax problem is mainly caused by different cirrus positions in various bands of the OLI image (Zhang et al., 2023), as can be seen in Fig. 2(b)–(f). Thus, this study simplifies the problem of cirrus parallax. The impact of cirrus clouds on different spectral bands decreases as the VNIR wavelength increases, resulting in distinct cirrus shapes and positions. The defference in cirrus clouds between different bands is considered cirrus parallax.

Fig. 2(g) shows the cirrus band of the OLI data, designed for cirrus cloud detection. However, a misalignment is observed mainly in the high-altitude cloud region, attributed to OLI sensor settings. The Landsat 8/9 OLI detector consists of fourteen Sensor Chip Assemblies (SCAs), including seven identical pairs of odd–even SCAs (Zanter, 2016). Overlapping regions exist between adjacent odd–even SCAs, however, the misalignment is primarily a result of the differing cirrus cloud positions in neighboring odd–even SCAs within the cirrus bands. Looking closely at Fig. 2(g), it is apparent that compared to the cirrus clouds in the visible bands, the position of the cirrus clouds on both sides of this strip is slightly lower on the left and slightly higher on the right.

Cirrus parallax correction is significant but challenging with model-based methods. To address the parallax issue, we divided the whole scene image into 14 image strips, including seven odd and seven even image strips. In this study, we adopted statistical methods to count the parallax laws based on the cirrus band between the VNIR and cirrus bands to correct the cirrus parallaxes. Then, it was found that there are two opposite cirrus parallax laws in an image, i.e., the cirrus parallax laws between VNIR and cirrus bands of the odd SCAs are opposite to that of the even SCAs. Since the types of pixels in the visible bands are very complex, the most effective approach is to correct the cirrus band according to parallax laws. Then, for each visible band, the new corresponding corrected cirrus band can be obtained.

Fig. 3 shows the process of parallax correction. Fig. 3(a) is the offset of the cirrus cloud position within the cirrus band from the cirrus cloud position within the VNIR band initially. Fig. 3(b) is the result after the cirrus band has been corrected to the left. Fig. 3(c) represents the final result after the cirrus band has been corrected. It should be noted that the near-infrared band is less affected by the thin cirrus cloud and that parallax occurs mostly in the visible bands so parallax correction is not required for the near-infrared band.

Because the parallax laws are related to the odd–even SCAs, the index map of the SCAs must be known if we want to achieve high-quality cirrus removal for whole remote sensing imagery. However, no standard index data are provided on the USGS website. Furthermore, processing a whole OLI image is a considerable challenge. To overcome this limitation, we found that the distribution of the satellite view azimuth angle (VAA) data provided by the USGS is similar to the SCA index map, as shown in Fig. 4(a). Then, we processed the angle coefficient file using the Landsat 8/9 angle calculation tool (l8_angles, https://landsat.usgs.gov/sites/default/files/documents/L8_ANGLES_2_7_0.tgz), provided on the official website. Since our purpose was to obtain the index map of the SCAs, we modified the tool to set the satellite azimuth calculation to 1. The initial index results for all SCAs can be obtained as Fig. 4(b), where the white area is 5730, the overlapping area is 2865 (the gray area) and the black area is 0. For the SCA overlapping area, there is no need to perform cirrus correction, so in this study, we set the value of 2865 to 0 to make it the same as the background value, and the value of 5730 was set to 1. The SCAs could be labeled as 1 to 14 regions using the connectivity principle. The connectivity regions were labeled as odd numbers for the odd SCAs and even numbers for the even SCAs. The final index map has three unique values, as shown in Fig. 4(c), where 0 is the background and SCA overlap of the image, appearing in black, 1 is the index for the odd SCA, appearing in gray, and 2 is the index for the even SCA, appearing in white.

4. Experiments

4.1. Comparison of cirrus removal results

To validate the effectiveness of the FRCR method, ICA(Shen et al., 2015), CR-NAPCT(Xu et al., 2019), and SLCC(Zhang et al., 2021) were also selected for comparison. It should be noted that CR-NAPCT uses a mask to segment the whole image and addresses cloudy pixels. The corrected pixels were combined with cloud-free pixels. In practice, we find a color disparity between cloud-free and corrected pixels. Therefore, we use a Poisson fusion method to post-process CR-NAPCT results. We calculate the cloud removal and reference pixels and assess the methods using the spectral angle mapper (SAM) (Yuhas, 1992) and structure similarity index measure (SSIM) (Wang et al., 2004). The SAM value is in the range [0, 1], the smaller the SAM, the higher spectral similarity; the SSIM value is in the range [-1,1], and the larger the SSIM, the higher the image structure consistency. Cloud-free images of adjacent time phases are selected as reference data. SAM and SSIM evaluate the spectral similarity and structural consistency between images.

Four Landsat 8/9 OLI sub-images showcasing diverse surface features were chosen for experiments, as demonstrated in Fig. 5(a) to Fig. 8(a). The cirrus removal results show that the cirrus clouds have been removed from the cloudy images. However, predominantly blue-violet parallaxes remain in the results, except for the FRCR results. According to the zoomed result (the geographic area in red box) displayed, the effect of cirrus parallaxes is effectively eliminated by FRCR. However, the residual cirrus parallax is noticeable in the results of the other three methods. From the visual perspective, the FRCR results are smoother and show clearer surface information.

Table 3 lists the quantitative evaluation of cirrus removal results for all methods, where the optimal results are in bold. In most cases, the ICA method performs poorly. The FRCR method outperforms the other methods in all the scenes. The SAM results shown in Fig. 5 are 0.1119 (cloudy vs. reference), 0.9602 (ICA vs. reference), 0.1113 (CR-NAPCT vs. reference), 0.0692 (SLCC vs. reference), and 0.0665 (FRCR vs. reference). The SAM results shown in Fig. 6 are 0.1698, 0.1000, 0.0996, 0.0960, and 0.0950, respectively. The SAM results shown in Fig. 7 are 0.1579, 0.1302, 0.1016, 0.0835, and 0.0802, respectively. The SAM results shown in Fig. 8 are 0.2172, 0.2055, 0.1398, 0.1385, and 0.1311, respectively. The lowest SAM values of 0.0665, 0.0950, 0.0802, and 0.1311 indicate that the spectral similarity between the cirrus removal results obtained using FRCR and the reference is better than that of the other methods. The SSIM results shown in Fig. 5 are 0.9787, 0.1985, 0.9356, 0.9912, and 0.9917, respectively. The SSIM results shown in Fig. 6 are 0.9556, 0.8298, 0.9667, 0.9756, and 0.9772, respectively. The SSIM results shown in Fig. 7 are 0.9607, 0.7957, 0.9775, 0.9828, 0.9832, respectively. The SSIM results shown in Fig. 8 are 0.8414, 0.8692, 0.9210, 0.9352, and 0.9384, respectively. The highest values are 0.9917, 0.9772, 0.9832, and 0.9384, respectively. The SSIM results indicate the structural consistency between the cirrus removal results

obtained using FRCR and the reference, which is also better than that of the other methods. Based on the results, it can be concluded that the FRCR method is capable of eliminating the cirrus parallax residuals which leads to improved image integrity, structural consistency, and spectral similarity. As a result, the images become smoother with more natural transitions and better color consistency. In summary, the FRCR method significantly enhances the overall quality of the images.

In addition, the different methods were tested using the whole image of scene 1 with various clouds and surface features. The results of cirrus removal for all methods are as Fig. 9. Most of the cirrus clouds have been removed from the whole image. The zoomed images provide a more detailed comparison, as displayed in Fig. 9(g) – (j). From the zoomed images, it can be seen that the manifestation of parallaxes is more pronounced in the complex cirrus structures, especially in their boundaries and interior regions. Thus, the residual parallaxes are not apparent in the results for the entire image but are obvious in the local areas. In comparison, the parallaxes have been corrected in the FRCR result. Table 4 provides the SAM and SSIM values for the cirrus cloud removal results compared to the reference data, with the optimal results in bold. The FRCR results appear to be significantly better than the other methods. It indicates that the FRCR results have higher spectral similarity and structural consistency. It is clear from the comparison results that the FRCR method is capable of handling the whole image, making it suitable for practical engineering applications.

4.2. Assessment of efficiency

The efficiency experiment was divided into two parts: 1) the time for solving γ; and 2) the total runtime of the program. A whole Landsat 8/9 OLI data was selected and divided into subsets of different sizes, which were 400 × 400, 800 × 800, 1600 × 1600, 3200 × 3200, and the raw size, respectively, for the experimental test. All methods employed were implemented using C/C++ or CUDA programming languages.

4.2.1. The time for solving γ

The SLCC and FRCR methods, which include γ calculation, are used. The experiment only compared the computational performance without data I/O. We recorded the computing time for solving γ in SLCC, FRCR, FRCR with Open Multi-Processing (OpenMP), and FRCR (with CUDA), respectively. Table 5 illustrates that the time required to solve γ increases exponentially with the size of the experimental data. When using the original image size as the test data, SLCC required 816.629 s (approximately 15 min) to solve γ. In contrast, FRCR took 152.185 s, showing an improvement of over six times when compared to SLCC. With OpenMP parallelism, the runtime of FRCR was reduced to 23.072 s, showing more than a six times improvement over the non-optimized FRCR. In addition, the GPU-based FRCR displayed an exceptionally rapid runtime of only 0.111 s, indicating a 1,370 times improvement over non-parallel optimization and about 207 times over FRCR with OpenMP parallelism. The comparison results show that GPU acceleration is effective, with a significant improvement in the speed of the intensive computation.

4.2.2. The total runtime of the program

The entire program includes data I/O and core processes. For the FRCR method, some solving that needs to be performed on the CPU, such as obtaining the SCA index map and the parallax correction, are optimized in parallel using OpenMP. The implemented methods, including ICA, CR-NAPCT, SLCC, and FRCR, were compared. It should be noted that the runtime of CR-NAPCT is without poisson fusion post-processing. The runtime of the methods has been listed in Table 6. It illustrates that the runtime of the entire program increases exponentially with the increasing image size. When the test data size is small, such as 400 × 400, the runtime differences between each method are not obvious. However, as the data size grows, the discrepancy between the methods becomes more evident, and the benefits of GPU-based parallelism become increasingly significant, leading to a considerable reduction in program runtime.

5. Conclusions

In conclusion, a fast and robust cirrus removal (FRCR) method has been proposed. FRCR can effectively eliminate the parallaxes in the corrected results of Landsat 8/9 images. An automatic sampling method in FRCR is proposed to replace manual sampling. The processing of a whole image is time-consuming, so FRCR adopts GPU-based parallelization to improve computational efficiency. Four group Landsat 8/9 images are selected as the test data. The SAM and SSIM are employed as the quantitative metrics to assess the effectiveness of the different cirrus removal methods. From the qualitative analysis, it has been demonstrated that the FRCR method is effective in removing the cirrus cloud in Landsat 8/9 images and that the cirrus parallaxes can also be eliminated. Quantitatively, the FRCR method achieves significantly smaller SAM values and greater SSIM values compared to ICA, CR-NAPCT, and SLCC. In addition, we compared the computational efficiency of each method on different test data sizes and found that the FRCR method achieved optimal performance with minimal time, especially for processing whole images. Faster and more robust cirrus cloud removal is achieved by FRCR, overcoming cirrus parallaxes and lower computational efficiency.

The FRCR method can effectively remove thin cirrus clouds. However, when dealing with thick cirrus clouds (close to thick clouds), the method may not accurately restore the feature or surface information below the clouds, and there will still be some cirrus information remaining. There are still some thin clouds that cannot be detected by the cirrus band, and this type of thin cloud cannot be removed by this method. The method is currently only applicable to Landsat 8/9 OLI data and cannot be applied to data from other sources. The odd–even SCA index map in FRCR is derived from satellite VAA data, which has high accuracy, but it would further improve the processing workflow if we could obtain the official SCA index map.

CRediT authorship contribution statement

Tao Jiang: Data curation, Formal analysis, Investigation, Methodology, Software, Validation, Visualization, Writing – original draft. **Huanfeng Shen:** Conceptualization, Funding acquisition, Project administration, Supervision, Writing – review & editing. **Huifang Li:** Funding acquisition, Project administration, Writing – review & editing. **Chi Zhang:** Formal analysis, Methodology, Supervision, Writing – review & editing. **Liying Xu:** Data curation, Writing – review & editing. **Dekun Lin:** Software, Writing – review & editing.

Declaration of competing interest

The authors declare that they have no known competing financial interests or personal relationships that could have appeared to influence the work reported in this paper.

Data availability

Data will be made available on request.

Acknowledgements

This work was supported by the National Natural Science Foundation of China (41971303), the National Key Research and Development Program of China (2022YFF1301103), the Fundamental Research Funds for the Central Universities of China (2042023kfyq04 and 2042022dx0002), the Open Fund of Hubei Luojia Laboratory (220100041).

References

Balz, T., Stilla, U., 2009. Hybrid GPU-based single-and double-bounce SAR simulation. IEEE Trans. Geosci. Remote Sens. 47, 3519–3529.

Chander, G., Markham, B.L., Helder, D.L., 2009. Summary of current radiometric calibration coefficients for Landsat MSS, TM, ETM+, and EO-1 ALI sensors. Remote Sens. Environ. 113, 893–903.

Chavez Jr, P.S., 1988. An improved dark-object subtraction technique for atmospheric scattering correction of multispectral data. Remote Sens. Environ. 24, 459–479.

Chen, S., Chen, X., Chen, J., Jia, P., Cao, X., Liu, C., 2015. An iterative haze optimized transformation for automatic cloud/haze detection of Landsat imagery. IEEE Trans. Geosci. Remote Sens. 54, 2682–2694.

Dessler, A., Yang, P., 2003. The distribution of tropical thin cirrus clouds inferred from Terra MODIS data. J. Clim. 16, 1241–1247.

Dowling, D.R., Radke, L.F., 1990. A summary of the physical properties of cirrus clouds. J. Appl. Meteorol. Climatol. 29, 970–978.

Drusch, M., Del Bello, U., Carlier, S., Colin, O., Fernandez, V., Gascon, F., Hoersch, B., Isola, C., Laberinti, P., Martimort, P., 2011. Sentinel-2: ESA's optical high-resolution mission for GMES operational services. Remote Sens. Environ. 120, 25–36.

Du, Y., Guindon, B., Cihlar, J., 2002. Haze detection and removal in high resolution satellite image with wavelet analysis. IEEE Trans. Geosci. Remote Sens. 40, 210–217.

Gao, B.C., Li, R.R., 2017. Removal of Thin Cirrus Scattering Effects in Landsat 8 OLI Images Using the Cirrus Detecting Channel. Remote Sens. 9.

Gao, B.C., Goetz, A.F., Wiscombe, W.J., 1993. Cirrus cloud detection from airborne imaging spectrometer data using the 1.38 μm water vapor band. Geophys. Res. Lett. 20, 301–304.

Gao, B.C., Kaufman, Y.J., Han, W., Wiscombe, W.J., 1998. Corection of thin cirrus path radiances in the 0.4–1.0 μm spectral region using the sensitive 1.375 μm cirrus detecting channel. J. Geophys. Res.: Atmos. 103, 32169–32176.

Gao, B.-C., Yang, P., Han, W., Li, R.-R., Wiscombe, W.J., 2002. An algorithm using visible and 1.38-/spl mu/m channels to retrieve cirrus cloud reflectances from aircraft and satellite data. IEEE Trans. Geosci. Remote Sens. 40, 1659–1668.

Gao, H., Zhu, X., Guan, Q., Yang, X., Yao, Y., Zeng, W., Peng, X., 2022. cuFSDAF: An Enhanced Flexible Spatiotemporal Data Fusion Algorithm Parallelized Using Graphics Processing Units. IEEE Trans. Geosci. Remote Sens. 60, 1–16.

Gordon, H.R., Wang, M., 1994. Retrieval of water-leaving radiance and aerosol optical thickness over the oceans with SeaWiFS: a preliminary algorithm. Appl. Opt. 33, 443–452.

He, X.Y., Hu, J.B., Chen, W., Li, X.Y., 2010. Haze removal based on advanced haze-optimized transformation (AHOT) for multispectral imagery. Int. J. Remote Sens. 31, 5331–5348.

Holland, P.W., Welsch, R.E., 1977. Robust regression using iteratively reweighted least-squares. Commun. Stat. Theory. Methods. 6, 813–827.

Jaramago, J.A.G., Paoletti, M.E., Haut, J.M., Fernandez-Beltran, R., Plaza, A., Plaza, J., 2019. GPU parallel implementation of dual-depth sparse probabilistic latent semantic analysis for hyperspectral unmixing. IEEE J. Sel. Top. Appl. Earth Obs. Remote Sens. 12, 3156–3167.

Lindholm, E., Nickolls, J., Oberman, S., Montrym, J., 2008. NVIDIA Tesla: A unified graphics and computing architecture. IEEE Micro 28, 39–55.

Lv, H., Wang, Y., Shen, Y., 2016. An empirical and radiative transfer model based algorithm to remove thin clouds in visible bands. Remote Sens. Environ. 179, 183–195.

Makarau, A., Richter, R., Müller, R., Reinartz, P., 2014. Haze Detection and Removal in Remotely Sensed Multispectral Imagery. IEEE Trans. Geosci. Remote Sens. 52, 5895–5905.

Mao, Z., Chen, J., Hao, Z., Pan, D., Tao, B., Zhu, Q., 2013. A new approach to estimate the aerosol scattering ratios for the atmospheric correction of satellite remote sensing data in coastal regions. Remote Sens. Environ. 132, 186–194.

Masek, J.G., Wulder, M.A., Markham, B., McCorkel, J., Crawford, C.J., Storey, J., Jenstrom, D.T., 2020. Landsat 9: Empowering open science and applications through continuity. Remote Sens. Environ. 248, 111968.

McHardy, T.M., Campbell, J.R., Peterson, D.A., Lolli, S., Garnier, A., Kuciauskas, A.P., Surratt, M.L., Marquis, J.W., Miller, S.D., Dolinar, E.K., Dong, X., 2022. GOES ABI Detection of Thin Cirrus over Land. J. Atmos. Oceanic Technol. 39, 1415–1429.

Meyer, K., Yang, P., Gao, B.-C., 2004. Optical thickness of tropical cirrus clouds derived from the MODIS 0.66 and 1.375-/spl mu/m channels. IEEE Trans. Geosci. Remote Sens. 42, 833–841.

Mitchell, O., Delp, E.J., Chen, P.L., 1977. Filtering to remove cloud cover in satellite imagery. IEEE Trans. Geosci. Electron. 15, 137–141.

Nickolls, J., Dally, W.J., 2010. The Gpu Computing Era. IEEE Micro 30, 56–69.

Owens, J.D., Houston, M., Luebke, D., Green, S., Stone, J.E., Phillips, J.C., 2008. GPU computing. Proc. IEEE 96, 879–899.

Plaza, A., Du, Q., Chang, Y.-L., King, R.L., 2011. High performance computing for hyperspectral remote sensing. IEEE J. Sel. Top. Appl. Earth Obs. Remote Sens. 4, 528–544.

Richter, R., Wang, X., Bachmann, M., Schläpfer, D., 2011. Correction of cirrus effects in Sentinel-2 type of imagery. Int. J. Remote Sens. 32, 2931–2941.

Sassen, K., Cho, B.S., 1992. Subvisual-Thin Cirrus Lidar Dataset for Satellite Verification and Climatological Research. J. Appl. Meteorol. Climatol. 31, 1275–1285.

Shen, H., Li, H., Qian, Y., Zhang, L., Yuan, Q., 2014. An effective thin cloud removal procedure for visible remote sensing images. ISPRS J. Photogramm. Remote Sens. 96, 224–235.

Shen, Y., Wang, Y., Lv, H., Qian, J., 2015. Removal of thin clouds in Landsat-8 OLI data with independent component analysis. Remote Sens. 7, 11481–11500.

Wang, Z., Bovik, A.C., Sheikh, H.R., Simoncelli, E.P., 2004. Image quality assessment: from error visibility to structural similarity. IEEE Trans. Image Process. 13, 600–612.

Winker, D.M., Hunt, W.H., McGill, M.J., 2007. Initial performance assessment of CALIOP. Geophys. Res, Lett, p. 34.

Wu, Z., Wang, Q., Plaza, A., Li, J., Sun, L., Wei, Z., 2015. Parallel spatial–spectral hyperspectral image classification with sparse representation and Markov random fields on GPUs. IEEE J. Sel. Top. Appl. Earth Obs. Remote Sens. 8, 2926–2938.

Wu, Z., Shi, L., Li, J., Wang, Q., Sun, L., Wei, Z., Plaza, J., Plaza, A., 2017. GPU parallel implementation of spatially adaptive hyperspectral image classification. IEEE J. Sel. Top. Appl. Earth Obs. Remote Sens. 11, 1131–1143.

Xia, L., Zhao, F., Chen, L., Zhang, R., Mao, K., Kylling, A., Ma, Y., 2018. Performance comparison of the MODIS and the VIIRS 1.38μm cirrus cloud channels using libRadtran and CALIOP data. Remote Sens. Environ. 206, 363–374.

Xu, M., Jia, X., Pickering, M., 2014. Automatic cloud removal for Landsat 8 OLI images using cirrus band, 2014 IEEE Geoscience and Remote Sensing Symposium, pp. 2511-2514.

Xu, M., Pickering, M., Plaza, A.J., Jia, X., 2015. Thin cloud removal based on signal transmission principles and spectral mixture analysis. IEEE Trans. Geosci. Remote Sens. 54, 1659–1669.

Xu, M., Jia, X., Pickering, M., Jia, S., 2019. Thin cloud removal from optical remote sensing images using the noise-adjusted principal components transform. ISPRS J. Photogramm. Remote Sens. 149, 215–225.

Yang, X., Chen, J., Guan, Q., Gao, H., Xia, W., 2022. Enhanced Spatial-Temporal Savitzky–Golay Method for Reconstructing High-Quality NDVI Time Series: Reduced Sensitivity to Quality Flags and Improved Computational Efficiency. IEEE Trans. Geosci. Remote Sens. 60, 1–17.

Young, S.A., Vaughan, M.A., Garnier, A., Tackett, J.L., Lambeth, J.D., Powell, K.A., 2018. Extinction and optical depth retrievals for CALIPSO's Version 4 data release. Atmos. Meas. Tech. 11, 5701–5727.

Yuhas, R.H., Goetz, A.F., Boardman, J.W., 1992. Discrimination among semi-arid landscape endmembers using the spectral angle mapper (SAM) algorithm, JPL, Summaries of the Third Annual JPL Airborne Geoscience Workshop. Volume 1: AVIRIS Workshop.

Zanter, K., 2016. Landsat 8 (L8) data users handbook. https://www.usgs.gov/media/files/landsat-8-data-users-handbook (accessed 23 January 2023).

Zhang, Y., Guindon, B., Cihlar, J., 2002. An image transform to characterize and compensate for spatial variations in thin cloud contamination of Landsat images. Remote Sens. Environ. 82, 173–187.

Zhang, C., Li, H., Shen, H., 2021. A scattering law based cirrus correction method for Landsat 8 OLI visible and near-infrared images. Remote Sens. Environ. 253, 112202.

Zhang, C., Li, H., Shen, H., He, H., Liu, Y., Yi, P., Xu, L., 2023. A General Thin Cloud Correction Method Combining Statistical Information and a Scattering Model for Visible and Near-infrared Satellite Images. IEEE Trans. Geosci. Remote Sens. 61, 1–19.